Articles

Hydrothermal Synthesis of Pure α-Phase Manganese(II) Sulfide without the Use of Organic Reagents

F. M. Michel,*[,†,‡] M. A. A. Schoonen,[†,‡] X. V. Zhang,[§] S. T. Martin,[§] and J. B. Parise[†,‡]

Center for Environmental Molecular Science (CEMS), Department of Geosciences, Stony Brook University, Stony Brook, New York 11794, and Division of Engineering and Applied Sciences, Harvard University, Cambridge, Massachusetts 02138

Received September 24, 2004. Revised Manuscript Received November 10, 2005

Recent studies exploring the role of metal sulfides as (photo)catalysts in prebiotic synthesis reactions provide the impetus for finding carbon-free synthesis methods for metal sulfides. The decomposition of organosulfur and organometallic precursor compounds is often the protocol for synthesizing bulk metal chalcogenides, such as manganese sulfide (MnS). Here we report a hydrothermal synthesis method for the formation of MnS in which a $MnCl_2$ solution is injected into a preheated sulfide solution. By varying the temperature of injection and subsequent aging time, we can control the specific crystal phase of the product. Three MnS polymorphs are known, and two of these, α-MnS and γ-MnS, form as pure phases in aqueous systems. The initial precipitate formed upon mixing of aqueous solutions of Mn^{2+} and S^{2-} at ambient temperature is nanocrystalline and is composed of a mixture of γ-MnS (wurtzite structure) and β-MnS (zinc blende structure). β-MnS has not previously been identified as forming under aqueous conditions. The initial binary-phase precipitate can be transformed to pure, highly crystalline γ-MnS by aging at temperatures as low as 150 °C within 3 days. Aging to yield pure α-MnS requires temperatures in excess of ∼200 °C for 3 days. Characterization of the products was performed using powder X-ray diffraction, total scattering and pair distribution function analysis, dynamic light scattering, and transmission and scanning electron microscopy. Chemical analyses were performed using colorimetric techniques.

1. Introduction

Manganese sulfide (MnS) occurs naturally as alabandite (α-MnS) and is the subject of recent photoelectrochemical research to test the hypothesis that MnS may have played a role in prebiotic synthesis on early Earth.[1] The use of crystalline MnS formed in the absence of any organosulfur compounds circumvents the introduction of additional sources of carbon in such photochemical studies. In this study we present an aqueous pathway to form pure α-MnS without the use of organosulfur reagents. Our findings are consistent with prior studies discussed below which indicated that the abundance of the various MnS phases precipitated by solvothermal methods was strongly dependent on reaction temperature and aging time. The formation of the thermodynamically stable α-phase is kinetically inhibited at room temperature; however, under solvothermal conditions this phase will form readily at temperatures in excess of ∼200 °C.

MnS crystallizes in one of three polymorphs, each with distinct physical and structural properties. The metastable beta (β) and gamma (γ) phases are pink and form at low temperatures with tetrahedrally coordinated zinc blende (space group $F\bar{4}3m$) and wurtzite (space group $P6_3mc$) crystal structures, respectively. The thermodynamically stable alpha (α) phase forms at a relatively higher temperature with an octahedrally coordinated rock salt structure (space group $Fm\bar{3}m$) and a green color. Early experimental work involving the magnetic, electrical, and optical properties of the MnS phases have been summarized elsewhere.[2]

Various procedures have been reported for the formation of MnS in one or more of the three polymorphic forms. These include the reaction of elemental Mn and S at elevated temperatures[3−5] and deposition in the form of films,[6−13] which, in at least one instance, was formed from the

[†] Department of Geosciences, Stony Brook University.
[‡] Center for Environmental Molecular Science, Stony Brook University.
[§] Harvard University.

(1) Zhang, X. V.; Martin, S. T.; Friend, C. M.; Schoonen, M. A. A.; Holland, H. D. *J. Am. Chem. Soc.* **2004**, *126*, 11247−11253.
(2) Rao, C. N. R.; Pisharody, K. P. R. *Prog. Solid State Chem.* **1976**, *10*, 207−270.
(3) Clendenen, R. L.; Drickamer, H. G. *J. Chem. Phys.* **1965**, *44*, 4223−4228.
(4) Sombuthawee, C.; Bonsall, S. B.; Hummel, F. A. *J. Solid State Chem.* **1978**, *25*, 391−399.
(5) Wiedemeier, H.; Sigai, A. G. *J. Cryst. Growth* **1969**, *6*, 67−71.
(6) Goede, O.; Heimbrodt, W.; Weinhold, V. *Phys. Status Solidi B* **1986**, *136*, K49.
(7) Goede, O.; Heimbrodt, W.; Weinhold, V.; Schnurer, E.; Eberle, H. G. *Phys. Status Solidi B* **1987**, *143*, 511.
(8) Jahne, E.; Goede, O.; Weinhold, V. *Phys. Status Solidi B* **1988**, *146*, K157.
(9) Praminik, P.; Akhter, M. A.; Basu, P. K. *Thin Solid Films* **1988**, *158*, 271−275.

10.1021/cm048320v CCC: $33.50
Published on Web 03/08/2006

Table 1. Sample Identifications, Synthesis Conditions, and Analyses

synthesis protocol	sample ID	mixing temp (°C)	heating time[a] (min)	aging temp (°C)	aging time (min)	phase	analyses presented: XRD	PDF	DLS	HACH
A	Inj-250	250	32	250	5	wur	X	X		X
	Inj-275	275	34	275	5	wur/rs	X			
	Inj-300	300	36	300	5	wur/rs	X			
	Inj-325	325	38	325	5	wur/rs	X			
	Inj-350	350	40	350	5	rs	X	X		X
A	Age-230A	RT	28	230	30	wur	X			
	Age-230B	RT	28	230	120	wur/rs	X			
	Age-230C	RT	28	230	180	wur/rs	X			
	Age-230D	RT	28	230	240	wur/rs	X			
	Age-230E	RT	28	230	360	rs	X	X		
B	Age-150	RT	20	150	3 days	wur		X		
B	Age-200	RT	25	200	3 days	rs		X		
–	RT-Fresh	RT	N/A	N/A	N/A	wur/zb	X	X	X	X

[a] Heating time equals the total time required to reach and stabilize at the mixing temperature designated. RT indicates reagents were initially mixed at room temperature (22 °C). XRD indicates data collected using Cu $K\alpha_1$ radiation. N/A indicates not applicable.

decomposition products of organometallic precursor compounds.[14] In several other experimental studies, MnS was initially formed from inorganic precursors under aqueous conditions but was then dried and later transformed to α-MnS by heating at elevated temperatures (1000 °C).[15,16] Prior studies have also reported the formation of both metastable polymorphs (β and γ) and stable (α) MnS using solvothermal synthesis techniques.[17−21] To our knowledge, synthesis of MnS in all such prior studies relied on the use of elemental components or on the thermal decomposition of an organic precursor at elevated temperature in combination with extended aging.[10,17,20,22,23] β-MnS, in particular, was previously observed to be formed only under nonaqeous conditions.[20] This phase has the lowest free energy of formation of the MnS polytypes, followed closely by that of the γ-phase. Lu et al.[17] succeeded in forming β-MnS in an ether solvent (tetrahydrofurane) and γ-MnS in a hydrocarbon solvent (benzene). Both of the solvents used in this case were nonaqueous and nonpolar. This observation suggests that the precipitation kinetics within the Mn−S system are strongly dependent on the polarity of the solvent and on slight differences in the surface tensions of the three polymorphs.

The synthesis method presented here may also be useful to other applications for which a carbon-free MnS, which is a dilute semiconductor material, is desirable. Carbon-free synthesis routes have recently been explored as part of research investigating the fabrication of bulk superconducting materials such as Bi-based compounds and other superconducting cuprates.[24] Studies on the synthesis of boron nitride nanostructures have also been hindered by carbon contamination due to the presence of carbon in the precursor reagents.[25]

2. Experimental Section

2.1. Synthesis of MnS Precipitates. Pure metastable (γ) and stable (α) MnS crystallites were precipitated using two different protocols. Reagent solutions were prepared and MnS products were extracted at room temperature (22 ± 2 °C) in a glovebox under a N_2 atmosphere. The resulting product slurry was filtered over a membrane filter with 0.2-μm or 0.45-μm pores. The MnS precipitate collected on the filter was dried at room temperature under a stream of N_2 prior to characterization.

2.1.1. MnS Synthesis: Protocol A. In one series of experiments using protocol A, the reagents were mixed by the rapid direct injection of 20 mL of room temperature 0.2 M $MnCl_2$ into 22 mL of 0.05 M sulfide solution (NaSH/NaOH), which had been preheated to an elevated temperature of 230 ± 5 °C using a hydrothermal mixing apparatus as described below. Experimental details including heating times required to reach stable reaction temperatures are included in Table 1. The injection apparatus consisted of a 42-mL stainless steel reaction vessel, injection pump, temperature control components, and associated plumbing. This type of injection method has been utilized for more than 15 years in the synthesis of iron sulfides and other hydrothermal studies.[26,27] The reacted solutions were then aged at the injection temperature (230 ± 5 °C) for periods ranging from 5 ± 0.5 min up to 6 ± 0.1 h. In a second series of experiments also using protocol A, the reagents were mixed at elevated temperatures, ranging from 250 to 350 ± 5 °C, and then "instantaneously" quenched to room temperature. Quenching was

(10) Lokhande, C. D.; Ennaoui, A.; Patil, P. S.; Giersig, M.; Muller, M.; Diesner, K.; Tributsch, H. *Thin Solid Films* **1998**, *330*, 70−75.
(11) Skromme, B. J.; Zhang, Y.; Smith, D. J.; Sivananthan, S. *Appl. Phys. Lett.* **1995**, *67*, 2690−2692.
(12) Sivananthan, S.; Wang, L.; Sporken, R.; Chen, J.; Skromme, B. J.; Smith, D. J. *J. Cryst. Growth* **1996**, *159*, 94−98.
(13) Okajima, M.; Tohda, T. *J. Cryst. Growth* **1992**, *117*, 810−815.
(14) Nomura, R.; Konishi, K.; Futenma, S.; Matsuda, H. *Appl. Organomet. Chem.* **1990**, *4*, 607.
(15) Banewicz, J. J.; Lindsay, R. *Phys. Rev.* **1956**, *104*, 318−320.
(16) Ahuja, L. D.; Rajeshwar, D.; Nagpal, K. C. *J. Colloid Interface Sci.* **1987**, *123*, 380−390.
(17) Lu, J.; Qi, P.; Peng, Y.; Meng, Z.; Yang, Z.; Yu, W.; Qian, Y. *Chem. Mater.* **2001**, *13*, 2169−2172.
(18) Jun, Y.; Jung, Y.; Cheon, J. *J. Am. Chem. Soc.* **2002**, *124*, 615−619.
(19) Zhang, Y.; Wang, H.; Wang, B.; Yan, H.; Yoshimura, M. *J. Cryst. Growth* **2002**, *243*, 214−217.
(20) Zhang, Y.-C.; Wang, H.; Wang, B.; Xu, H.-Y.; Yan, H.; Yoshimura, M. *Opt. Mater.* **2003**, *23*, 433−437.
(21) Kennedy, S. W.; Harris, K.; Summerville, E. *J. Solid State Chem.* **1980**, *31*, 355−359.
(22) Wang, S.; Li, K.; Zhai, R.; Wang, H. *Mater. Chem. Phys.* **2005**, *91*, 298−300.
(23) Joo, J.; Na, H. B.; Yu, T.; Yu, J. H.; Kim, Y. W.; Wu, F.; Zhang, J. Z.; Hyeon, T. *J. Am. Chem. Soc.* **2003**, *125*, 11100−11105.
(24) Tang, C. C.; Bando, Y.; Sato, T. *Appl. Phys. A* **2002**, *75*, 681−685.
(25) Tong, T. B.; Li, C. R. *Chin. J. Phys.* **1998**, *36*, 280−287.
(26) Poulson, S. R.; Schoonen, M. A. A. *Chem. Geol.* **1994**, *116*, 305−315.
(27) Schoonen, M. A. A.; Barnes, H. L. *Geochim. Cosmochim. Acta* **1991**, *55*, 3491−3504.

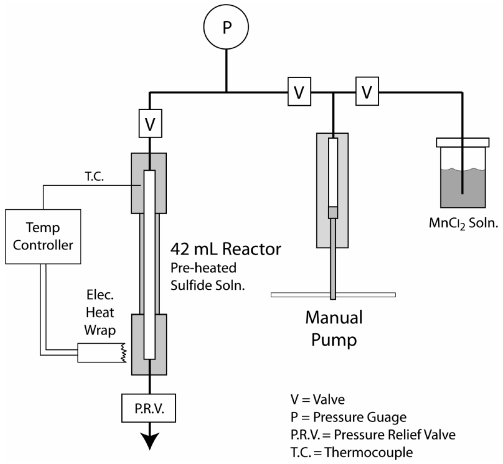

Figure 1. Hydrothermal mixing apparatus. A $MnCl_2$ solution is drawn into a manual injection pump while the sulfide solution is preheated to a desired reaction temperature in the 42-mL reaction vessel. The vessel, constructed of 316SS, is heated using electric heat wrap and maintained using an electronic temperature controller and Variac. A pressure relief valve allows the escape of some fluid due to heating and volume expansion and the displacement of the sulfide solution at the time of injection of $MnCl_2$ (22 mL). The injection pressure is monitored using an in-line pressure gauge. The temperature of the vessel is monitored using a thermocouple connected to the controller unit.

achieved by immersion of the sealed reaction vessel into a water bath at room temperature within approximately 5 min of mixing. (As a result of the physical limitations of the injection apparatus, a short period of aging was inevitable but was limited to 5 ± 0.5 min from injection to quenching.) Each run remained in the room temperature water bath for a minimum of 20 min, and a temperature probe was used to verify that the reactor body thermally equilibrated with the water in the bath. A reduced concentration of the sulfide solution was employed in this protocol because of the corrosiveness of sulfide in stainless steel at elevated temperature.

2.1.2. MnS Synthesis: Protocol B. In protocol B, the reagents (20 mL of 0.2 M $MnCl_2$ into 42 mL of 0.2 M sulfide solution) were mixed at room temperature (22 ± 5 °C) using the same hydrothermal mixing apparatus as above and subsequently heated to and aged at elevated temperature. Experimental details are again included in Table 1. In this protocol, the initial precipitate formed upon mixing of aqueous solutions of Mn and S at room temperature is a binary mixture of γ- and β-MnS. This precipitate is characterized as a part of this study. The poorly crystalline initial precipitate was subsequently heated to and aged at temperatures of 150 or 200 ± 5 °C for 72 ± 0.25 h, thereby forming highly crystalline γ- or α-MnS, respectively.

2.1.3. Chemicals. $MnCl_2 \cdot 4H_2O$ (99%) and $Na_2S \cdot 9H_2O$ (99%; hereafter referred to as NaSH/NaOH or sulfide) were from Fisher Chemicals. The chemicals were analytical grade and were used as received without additional purification. Solutions were prepared using water that was deionized (EasyPure, filtered 0.2 μm, UV/UF) and purged with N_2 (99.99% pure) for at least 30 min to remove dissolved molecular oxygen.[28]

2.1.4. Hydrothermal Apparatus. The hydrothermal apparatus used in this study is based on a rapid injection design described in earlier work.[26,27] In brief, a 42-mL tube reactor was connected to a manual, high-pressure generator pump and a pressure relief valve (Figure 1). This pump was used to inject one of the reagents, here $MnCl_2$, into the reactor vessel containing the preheated sulfide solution (protocol A only). A pressure relief valve was used to suppress boiling of the preheated sulfide solution before the $MnCl_2$ solution was injected using the hand pump. The relief valve also allowed some of the fluid to escape as a result of volume expansion during heating and the injection. The backpressure on the relief valve was set at 250 ± 10 bar. The reactor (High Pressure Equipment Company (HiP)), relief valve (Swagelok), hand pump (HiP), and connecting tubing were made out of 316 stainless steel. The reactor was heated using a heavy-duty, insulated electric heat tape wrapped around the body of the reactor. The temperature of the reactor was maintained using a thermocouple-controller unit.

Table 2. General Protocols (A and B) for Product Syntheses

step	action
synthesis	load sulfide solution in the 42-mL stainless steel reaction vessel and preheat to desired reaction temperature (heating in protocol A only) inject $MnCl_2$ solution aging at elevated injection temperature for periods ranging from <5 min to 6 h (protocol A only); heating to and aging at elevated temperatures ranging from 150 to 200 ± 5 °C for 3 days (protocol B only) quenching and extraction of liquid and solid (slurry) under N_2 atmosphere
rinse cycle 1	centrifuge initial slurry 5 min at 5000 rpm decant supernatant and add ~45 mL of 1 mM sulfide solution sonicate (1 min) and vortex (20 s)
rinse cycle 2	repeat cycle 1
rinse cycle 3	centrifuge 5 min at 5000 rpm decant supernatant[a]
extraction	filter solid-phase product dry product under N_2 stream
XRD mounts	low-energy: powders mixed into amorphous silicone grease to inhibit oxidation and mounted on glass slides high-energy: powders loaded dry into 1 mm polyimide capillaries and capped with glass wool and epoxy
EM mounts	product mounted directly from colloidal suspensions obtained during rinse cycle 3[a] onto aluminum stubs (SEM) or carbon-coated, Cu grids (TEM)

[a] Supernatant included a stable suspension of colloidal MnS particles and was preserved for electron microscopic imaging. Note: During the rinse cycles described the samples were sealed in a centrifuge tube and capped with a H_2-N_2 mix. Samples for DLS measurements were also prepared using the colloidal suspension from rinse cycle 3.

2.2. Characterization of MnS Precipitates. Characterization of the run products was carried out by X-ray diffraction XRD, transmission and scanning electron microscopy (TEM and SEM), and/or pair distribution function (PDF) analysis analysis. Dynamic light scattering (DLS) was also attempted to determine the particle size distribution. The poorly crystalline initial precipitate formed upon mixing of aqueous solutions of Mn and S at room temperature was also characterized. Total scattering data from high-energy synchrotron radiation and for PDF analysis were collected on selected samples. Total-Fe contents in selected run products and their starting reagents were determined using colorimetric techniques. Sample identification and an overview of syntheses and characterization are described in Tables 1 and 2.

2.2.1. X-ray Powder Diffraction (Cu Kα_1 Radiation). Once dry, MnS powder samples inside the glovebox were thoroughly mixed with an amorphous silicone vacuum grease to inhibit oxidation during slide preparation and XRD analysis. Powder XRD patterns were collected using a Scintag PADx diffractometer equipped with graphite monochromatized Cu Kα_1 radiation ($\lambda = 1.5405$ Å) and a scanning rate of 2.0°/min with 2θ ranging from 20 to 75°. The use of the silicone grease resulted in a background interference and created a "hump" in the intensity spectrum at low 2θ. The

(28) Butler, I. B.; Schoonen, M. A. A.; Rickard, D. T. *Talanta* **1994**, *41*, 211−215.

Table 3. PDF Model Refinement Results

parameter	Age-150[a] (wur)	Inj-250[b] (wur)	γ-MnS[c]	Age-200[b] (rs)	Inj-350[b] (rs)	α-MnS[d]	CeO_2[a]	CeO_2[b]
a (Å)	3.987(4)	3.974(9)	3.987	5.213(4)	5.213(8)	5.222(6)	5.407(0)	5.419(9)
c (Å)	6.457(6)	6.430(3)	6.438					
S z position (Å)	0.3763(3)	0.3762(3)	0.375					
R_w (%)	19.9	17.4		17.6	10.5		28.9	17.5
σ_Q ($Å^{-1}$)	0.036(1)	0.050(8)		0.028(3)	0.042(0)		0.033(3)	0.032(8)
δ	0.0756	0.104(9)		0.061(0)	0.071(4)		0.034(3)	0.053(6)
U_{Mn}[e] ($Å^2$)	0.010(2)	0.012(7)		0.008(3)	0.013(0)		0.006(1)	0.004(5)
U_S[e] ($Å^2$)	0.010(3)	0.012(6)		0.008(8)	0.013(0)		0.008(8)	0.023(7)
aging	72 h at ~150 °C	5 min at ~250 °C		72 h at ~200 °C	5 min at ~350 °C			

[a] Indicates data collected at 1-ID (energy = 79.9 keV). [b] Indicates data collected at 1-ID (energy = 99.9 keV). "wur" and "rs" indicate fitting of the wurtzite (γ-MnS) and rock salt (α-MnS) models, respectively. [c] Cell parameters reported in ICSD-44765 for crystalline γ-MnS. [d] Cell parameters reported in ICSD-76204 for crystalline α-MnS. [e] *U* = isotropic-displacement parameter.

atomic structure types of the run products formed at elevated temperatures using protocols A and B were determined using powder XRD techniques and comparison of the experimental patterns with the Joint Committee on Powder Diffraction Standards (JCPDS) database.

2.2.2. High-Energy Powder XRD at the Advanced Photon Source (APS). Selected powdered samples (RT-Fresh, Inj-250, Inj-350, Age-150, Age-200) were loaded into 1 mm o.d. polyimide (Kapton) capillaries under a completely anoxic atmosphere and capped at both ends with glass wool and epoxy so as to inhibit oxidation. The loaded capillaries were then sealed under anoxic conditions in glass culture tubes with septum caps and transported to the APS. High-energy XRD data were collected at the 1-ID beamline (99.9 keV, $\lambda = 0.1240$ Å, or 79.9 keV, $\lambda = 0.1551$ Å)[29] of the APS. A CeO_2 standard (NIST diffraction intensity standard set: 674a) was used to calibrate the sample-to-detector distance and the tilt of the detector relative to the incident beam path. The energy calibration was initially achieved using the gold absorption edge as reference and, if increased to higher energies (i.e., 99.9 keV), was recalibrated by refinement of the wavelength and fixing of the sample-to-detector distance. The radiation scattered by the calibrant and samples was collected on a MAR-345 image plate detector system and processed using the program Fit-2D.[30,31] A polarization factor was applied during integration of the data. Data were also collected for an empty polyimide capillary (1 mm o.d.) for background correction during PDF analysis.

2.2.3. PDF Analysis. The total scattering structure function $S(Q)$ and PDF $G(r)$ were obtained using PDFgetX2[32] where standard corrections were applied as well as those unique to image-plate geometry.[33] The Fourier transform of the normalized and weighted $S(Q)$, or $Q[S(Q) - 1]$, results in the PDF, or $G(r)$, which corresponds to real-space interatomic distances. The unit cells for crystalline α- and γ-MnS each consist of two Mn and two S atoms. The unit cell for crystalline β-MnS consists of four Mn and four S atoms. The initial atomic coordinates, cell parameters, isotropic displacement parameters (U), and spacegroups $Fm\bar{3}m$, $P6_3mc$, and $F\bar{4}3m$ are those of the JCPDS database Powder Diffraction File Nos. 6-518, 40-1289, and 40-1288 for α-, γ-, and β-MnS polymorphs, respectively. The models for the crystalline MnS polymorphs are fitted to the experimental PDFs, and the structural parameters of each model are refined and plotted using the programs PDFfit and Kuplot,[34] respectively. Unit cell parameters, isotropic-displacement parameters, atom positions, resolution dampening (σ_Q), a peak sharpening factor (δ), and a scale factor were refined simultaneously using PDFFit. A "goodness of fit" indicator (R_w) is reported for each refinement (Table 3). The two additional parameters δ and σ_Q are incorporated in the refinements to model the sharpening of the PDF near neighbor peaks due to correlated motion between atom pairs (δ) and the exponential decay of the PDF (σ_Q), respectively. The exponential decay of the PDF can, in certain cases, be attributed to a limited range of structural coherence in nanocrystalline materials, that is, minimum average crystallite size.[35−38] In the case of highly crystalline samples, the exponential decay is primarily an indication of the resolution of the instrument[37] or instrument envelope. A crystalline CeO_2 standard was also analyzed during each of the two data collection events, and the results of the PDF refinements are included for comparison (Table 3).

2.2.4. DLS. Particle sizes of the initial precipitate were measured using DLS techniques with a Brookhaven Instruments Corporation 90Plus/BI-MAS particle size analyzer. The intensity correlation function of this sample was measured over five runs at a scattering angle of 90° from the incident laser beam (695 nm). Particle sizing by DLS is a noninvasive technique whereby the diffusion of particles in solution is measured through light scattering. As a result, samples can be examined under aqueous conditions. Particle sizes ranging from 150 to 10 000 nm were determined from the autocorrelation function based upon the CONTIN[39] and non-negative least squares[40] analysis procedures.

2.2.5. SEM and TEM. Run products selected for analysis by SEM and energy dispersive analysis using X-rays (EDAX) were extracted directly from the reaction vessel and drawn through a 0.2-μm polypropylene filter. The products were then washed with deionized water free of molecular oxygen and dried at room temperature using a stream of N_2. The solid-phase precipitate was then re-dispersed in ethanol and mounted on aluminum stubs. SEM was performed using a Leo 1550 equipped with a Schottky Field Emitting Gun and an EDAX Phoenix system. TEM imaging was performed on

(29) Shastri, S. D.; Fezzaa, K.; Mashayekhi, A.; Lee, W.-K.; Fernandez, P. B.; Lee, P. L. *J. Synchrotron Radiat.* **2002**, 317−322.
(30) Hammersley, A. P. *FIT2D, version 9.129, Reference Manual, version 3.1*; ESRF Internal Report, ESRF98HA01T; European Synchrotron Radiation Facility: Grenoble, France, 1998.
(31) Hammersley, A. P.; Svenson, S. O.; Hanfland, M.; Hauserman, D. *High Pressure Res.* **1996**, *14*, 235−248.
(32) Qiu, X.; Thompson, J. W.; Billinge, S. J. L. *J. Appl. Crystallogr.* **2004**, *37*, 678.
(33) Chupas, P. J.; Qui, X.; Hanson, J. C.; Lee, P. L.; Grey, C. P.; Billinge, S. J. L. *J. Appl. Crystallogr.* **2003**, *36*, 1342−1347.
(34) Proffen, T.; Billinge, S. J. L. *J. Appl. Crystallogr.* **1999**, *32*, 572−575.
(35) Hall, B. D.; Zanchet, D.; Ugarte, D. *J. Appl. Crystallogr.* **2000**, *33*, 1335−1341.
(36) Billinge, S. J. L.; Petkov, V.; Proffen, Th. Structure of different length scales from powder diffraction: the real-space pair distribution function (PDF) technique. *Commission on Powder Diffraction of the International Union of Crystallography Newsletter*, 2000, no. 24.
(37) Page, K.; Proffen, T.; Terrones, H.; Terrones, M.; Lee, L.; Yang, Y.; Stemmer, S.; Seshadri, R.; Cheetham, A. K. *Chem. Phys. Lett.* **2004**, *393*, 385−388.
(38) Neder, R. B.; Korsunskiy, V. I. *J. Phys.: Condens. Matter* **2005**, *17*, S125−S134.
(39) Provencher, S. W. *Comput. Phys. Commun.* **1982**, *27*, 213−227.
(40) Morrison, I. D.; Grabowski, E. F.; Herb, C. A. *Langmuir* **1985**, *1*, 496−501.

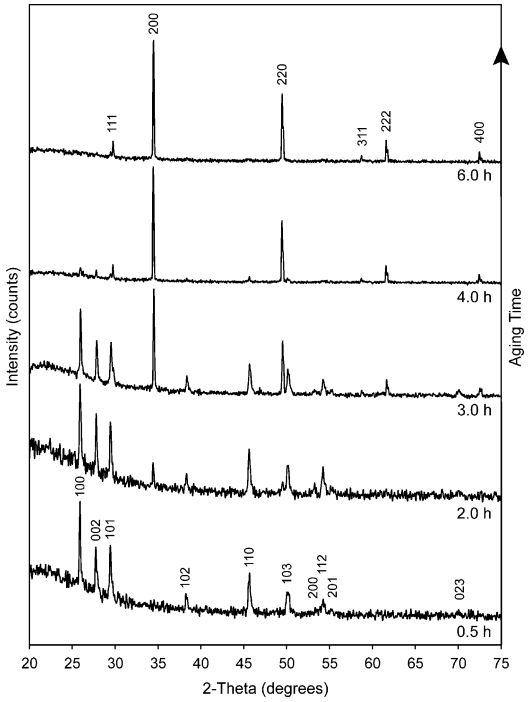

Figure 2. XRD for five MnS samples synthesized using protocol A. Mixing and aging occurred at 230 °C with aging times ranging from 0.5 to 6.0 h. Aging time increases from the bottom to the top plot. MnS samples with shorter amounts of aging (0.5 and 2.0 h) are dominantly γ-phase, whereas samples aged 4.0 and 6.0 h are dominantly α-MnS.

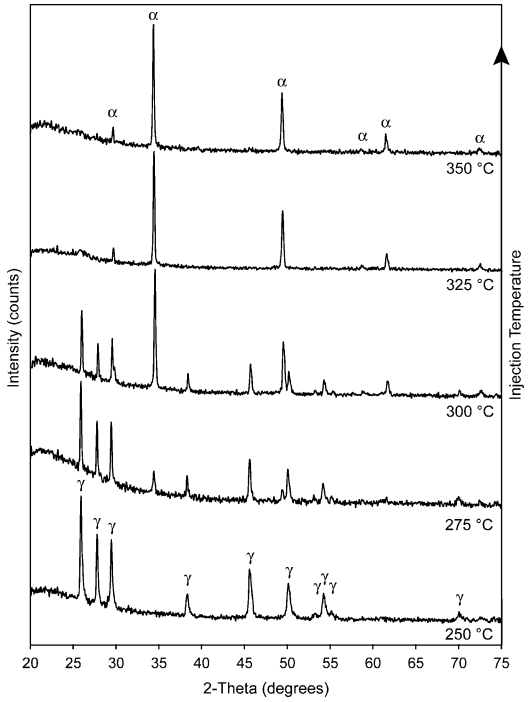

Figure 3. XRD for five MnS samples synthesized using protocol A by injection at temperatures ranging from 250 to 350 °C and aged less than 5 min. The injection temperature increases from the bottom to the top plot.

freshly precipitated MnS particles (RT-Fresh) using a Philips CM12 scanning TEM with a high brightness (LaB_6) electron gun. Colloidal MnS particles in solution were transferred under completely anoxic conditions, as described in Table 2, onto 300-mesh, 3-mm, carbon-coated copper grids with Formvar and lacey carbon support film. The mounted grids were dried under a stream of N_2, then stored temporarily in glass vials, and capped under anoxic conditions for transport to the transmission electron microscope. The grids were each exposed to atmospheric oxygen for less than 1 min on average, while being transferred from the vials to a beryllium TEM sample holder, before being placed under high vacuum in the microscope.

2.2.6. Chemical Analyses. Selected run products, dissolved in HCl (6 N) from Fisher Chemicals (Certified ACS Plus), were analyzed for total-iron content via colorimetric techniques using a HACH DR/4000 UV−vis spectrophotometer and HACH method 8147. Total-iron content was determined using the FerroZine fluorescence method ($\lambda = 562$ nm). The estimated minimum detection limit was 0.004 mg/L. The FerroZine iron reagent forms a purple-colored complex with trace amounts of iron in samples that are buffered to a pH of 3.5. The color change is directly proportional to the concentration of iron present. Less than 0.5 g of each of the solid-phase precipitates was dissolved in HCl. The precursor reagents at the same concentrations used in the syntheses were also analyzed to check for iron impurities.

3. Results and Discussion

Pure α-MnS was formed hydrothermally using both experimental protocols presented here. In one series of experiments using protocol A, α-MnS was formed via structural transformation of the metastable γ-phase after sufficient aging (6 h) at 230 ± 5 °C. Figure 2 presents XRD patterns for MnS formed using protocol A by direct injection at 230 ± 5 °C and subsequent aging for 0.5, 2, 3, 4, and 6 h. The patterns for samples aged for 2, 3 and 4 h show that both the α- and γ-phases are present simultaneously during the transition as a binary mixture. Here the abundance of α-phase crystals increases with aging time at the expense of the γ-phase. At 6 h the phase transition is complete, and only the thermodynamically stable α-phase is detectable.

In a second series of experiments also using protocol A, α-MnS was formed this time by injection at temperatures in excess of ∼325 °C. MnS samples were precipitated at temperatures ranging from 250 ± 5 to 350 ± 5 °C. The aging time was limited to approximately 5 min. The XRD results indicate that, at temperatures between ∼275 and ∼325 °C, the products consist of a binary mixture of α- and γ-MnS with the relative abundance of the α-phase increasing with reaction temperature (Figure 3). Above 325 °C, the precipitate is pure α-MnS, which suggests that either the nucleation barrier for this phase has been overcome or the transformation of γ-MnS to α-MnS is completed within as little as 5 min at this temperature. The design of the current study is not suited to resolve these two possibilities.

For MnS precipitated by protocol B (i.e., mixing of reactants at room temperature), the initial precipitate, without any subsequent aging at elevated temperature, is a binary mixture of the two metastable MnS polymorphs. The crystallinity of the initial precipitate is relatively poor, that is, having broadened and weak XRD reflections and a rapid rate of oxidation upon exposure to air. These features are attributable to extremely small particle sizes which result from rapid and frequent nucleation at the time of mixing.[41] Also contributing to the broadened maxima may be the effects of defects in the structures. The crystallinity of the initial metastable MnS precipitate improved when subsequent

(41) Waychunas, G. A. In *Nanoparticles and the environment*; Banfield, J. F., Navrotsky, A., Eds.; The Mineralogical Society of America: Washington, DC, 2001; Vol. 44, pp 105−162.

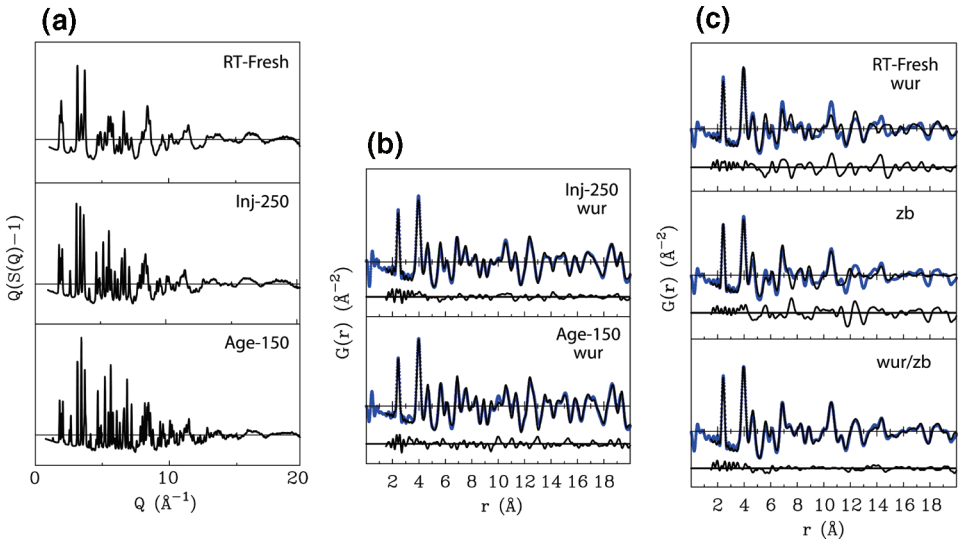

Figure 4. (a) Weighted total scattering structure function $Q[S(Q) - 1]$ for the run products (RT-Fresh, Inj-250, Age-150). (b) PDF $G(r)$ versus distance r plotted with the experimental data (blue circles) fitted by the refined model PDF (solid black) shown for samples Inj-250 and Age-150. The structure model for wurtzite (γ-MnS) is indicated by "wur". A difference plot is included beneath each data set as an indication of fit. (c) PDF $G(r)$ versus distance r plotted with the experimental data (blue circles) fitted by the refined model PDF (solid black) shown for sample RT-Fresh. The structure models for wurtzite (γ-MnS) and zinc blende (β-MnS) are indicated by "wur" and "zb". A difference plot is included beneath each PDF as an indication of fit.

aging occurred at 150 °C (sample: Age-150), as is indicated by a sharpening of the Bragg reflections and a relative increase in intensity. Sufficient aging at temperatures of 200 °C or higher using protocol B led to a complete structural transformation to form α-MnS (sample: Age-200).

3.1. Atomic Structure from PDF. Selected samples (RT-Fresh, Inj-250, Inj-350, Age-150, and Age-200) were evaluated using total scattering data and PDF analysis. Recently this technique has been applied successfully to studies of nanocrystalline materials for which traditional XRD techniques are limited (see appendix).[42,43,37] Several of these samples were anticipated to have dominantly nanosized crystallites due to the lack of aging at the elevated mixing temperatures (Inj-250 and Inj-350) or lack of both heating and aging (RT-Fresh). For comparison, highly crystalline γ-MnS (Age-150) and α-MnS (Age-200) were formed through extended aging at elevated temperatures, and for these cases the cell parameters derived from PDF refinement are nearly identical with those reported for these phases in the JCPDS database (Table 3). The PDF model fits for Inj-250 (Figure 4b) and Inj-350 (Figure 5b) and the refined cell parameters (Table 3) indicate that these samples also are highly crystalline. This result was somewhat unexpected because these two samples experienced very short aging times and thus were anticipated to be extremely fine-grained. As discussed further below, the presence of nanosized particles in either sample cannot be ruled out by PDF analysis alone because the PDF signal in a sample with a nonuniform distribution of particle sizes is dominated by the highly crystalline (largest) fraction. Therefore, electron imaging was also used to directly evaluate the distribution of particles sizes (see below).

In contrast to the highly crystalline run products, there are distinct regions of the PDF where the initial precipitate

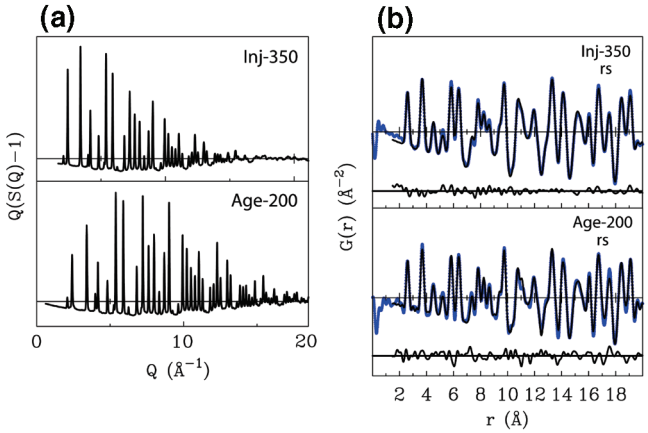

Figure 5. (a) Weighted total scattering structure function $Q[S(Q) - 1]$ for α-MnS run products (Inj-350, Age-200). (b) PDF $G(r)$ versus distance r plotted with the experimental data (blue circles) fitted by the refined model PDF (solid black) shown for samples Inj-350 and Age-200. The structure model for cubic rock salt (α-MnS) is indicated by "rs". A difference plot is included beneath each PDF refinement set as an indication of fit.

(RT-Fresh) is not adequately described on the basis of the structure of a single-phase model for either metastable polymorph. The top two panes in Figure 4c show the individual fits for wurtzite ("wur") and zinc blende ("zb"). Although the three nearest-neighbor atom pairs have a satisfactory fit by either model, there are obvious differences in peak positions and intensities at greater distances ($r >$ ~4 Å), as indicated in the difference plots. The presence of a binary mixture of the metastable polymorphs is testable by fitting the experimental PDF with a dual-phase ("wur/zb") model (Figure 4c, bottom pane). The fit is significantly improved, as indicated in the difference plot and the refinement results (Table 4). The ability to fit the data with two end-member structures, each based on a periodic model, suggests the presence of two separate and coherently scattering phases. The scaling factors, refined individually for each phase, indicate a wurtzite to zinc blende ratio of approximately 2:1.

(42) Michel, F. M.; Antao, S. M.; Chupas, P. J.; Lee, P. L.; Parise, J. B.; Schoonen, M. A. A. *Chem. Mater.* **2005**.
(43) Gilbert, B.; Huang, F.; Hengzhong, Z.; Waychunas, G. A.; Banfield, J. F. *Science* **2004**, *305*, 651−654.

Table 4. PDF Model Refinement Results (RT-Fresh)

	single-phase				dual-phase (wur/zb)	
parameter	γ-MnS (wur)	γ-MnS[a]	β-MnS (zb)	β-MnS[b]	γ-MnS (wur)	β-MnS (zb)
a (Å)	3.972(1)	3.987	5.617(6)	5.606	3.969(9)	5.615(9)
c (Å)	6.427(3)	6.438			6.440(2)	
S z position (Å)	0.382(1)	0.375			0.378(2)	
R_w (%)	38.8		41.3		16.0	
σ_Q (Å^{-1})	0.080(2)		0.142(1)		0.071(2)	
δ	0.67(3)		0.74(8)		0.55(6)	
U_{Mn}[c] (Å^2)	0.014(2)		0.015(1)		0.015(1)	0.019(5)
U_S[c] (Å^2)	0.023(4)		0.029(3)		0.015(7)	0.027(3)
scale factor (%)	74		77		51	26

[a] Cell parameters reported in ICSD-44765 for crystalline γ-MnS. [b] Cell parameters reported in ICSD-44764 for crystalline β-MnS. [c] U = isotropic-displacement parameter.

The exact spatial relationship between the two MnS phases coexisting in the initial precipitate is not presently known. An alternative to the presence of a binary mixture of discrete phases would be zinc blende occurring as intergrowths or defects in a wurtzite host structure (e.g., stacking faults or core−shell type nanoparticles). In the wurtzite structure, the occurrence of stacking faults are equivalent to alternating layers of wurtzite (ABAB stacking) and the closely related zinc blende structure (ABCABC stacking). This type of configuration is commonly observed in nanocrystalline CdSe,[44] ZnSe,[45] ZnO,[46] and ZnS.[46] Such planar defects in crystalline materials result in modifications in the intensities of specific peaks (e.g., [002] in zinc blende and [111] in wurtzite) as well as additional diffraction features, which are manifestations of the relationship between the two structure types. These features usually occur at slightly larger d spacing with relatively less intensity. As a result of peak broadening in the raw diffraction data any extra features become obscured by neighboring and often overlapping reflections. Such is the case in the initial nanocrystalline MnS precipitate (Figure 4a, top panel). Furthermore, in the case of extremely small particles, where the coherence length of the X-rays is comparable to the size of the intimately intergrown phases, the overall scattering would be distinct from these phases occurring separately. Under such conditions, a satisfactory fit of the PDF would not be obtained by two separate models, each based on a periodic structure.

3.2. Crystal Morphology. The morphology of the highly crystalline run products formed using both experimental protocols was evaluated by SEM. The α-MnS crystallites precipitated by injection at room temperature and aging at elevated temperature (protocol B) were octahedrons having abundant intergrowths and twins (Figure 7a). Increasing the injection temperature to 325 °C (protocol A) led to a morphology of the α-phase dominated by truncated cubes (Figure 7b). Although Figure 7c shows a nearly complete cube intergrown between two larger octahedrons, fully formed cubes were rare in the α-MnS samples examined and formed using either experimental protocol. This result was possibly due to insufficient aging time. The γ-MnS sample formed using protocol A and examined by SEM had varied crystal sizes and morphologies and was in general dominated by hexagonal prisms and dihexagonal pyramids (Figure 8a,b). The latter forms were bullet-shaped with varying dimensions. This morphology has also been observed in earlier studies.[23] Low-resolution TEM images of the nonaged sample precipitated at room temperature (RT-Fresh) indicated a dominance of extremely small crystallites of 5 to 10 nm. The dominant morphology was difficult to discern at this resolution but appeared irregularly shaped in general (Figures 9 and 10).

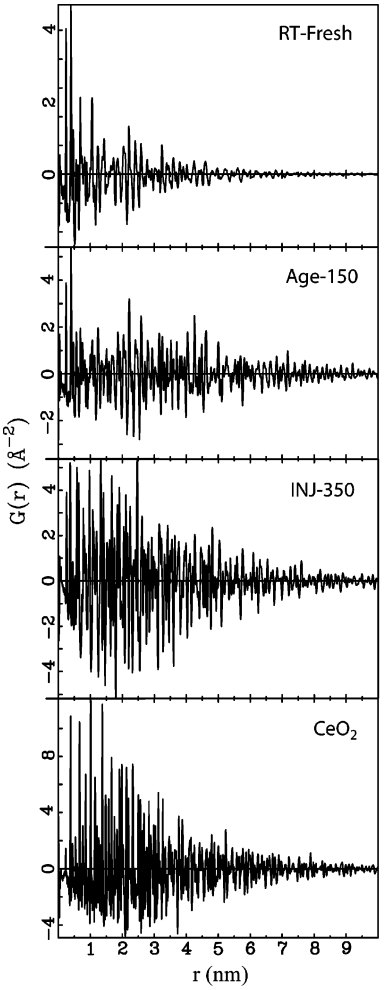

Figure 6. PDF $G(r)$ plotted out to 50 Å to illustrate the degree of attenuation due to the range of structural coherence (i.e., crystallite size) of the initial γ-MnS precipitate. The PDF for CeO_2 is also included to demonstrate the attenuation of a crystalline sample due to instrument resolution (1-ID). There is increased intensity and range in the correlations in the crystalline material.

3.3. Crystallite Size. In the present study crystallite sizes in selected samples were evaluated primarily using electron microscopy (SEM or TEM). A wide size distribution of highly crystalline MnS in both polymorphic forms was observed by SEM in the run products from both protocol A and protocal B (Figures 7a and 8b). Individual crystallite sizes in these samples ranged from tens of nanometers up to and exceeding 1 μm. Although all of the run products inspected by SEM were filtered (0.2-μm), nanosized particles were still visible (Figures 7a,c and 8a, arrows). Nanosized particles would be expected to pass through a 0.2-μm filter, and their presence may be in part due to a reduction in the

(44) Manna, L.; Scher, E. C.; Alivisatos, A. P. *J. Am. Chem. Soc.* **2000**, *122*, 12700−12706.
(45) Hu, J.; Bando, Y.; Liu, Z.; Sekiguchi, T.; Golberg, D.; Zhan, J. *J. Am. Chem. Soc* **2003**, *125*, 11306−11313.
(46) Ding, Y.; Wang, Z. L. *J. Phys. Chem. B* **2004**, *108*, 12280−12291.

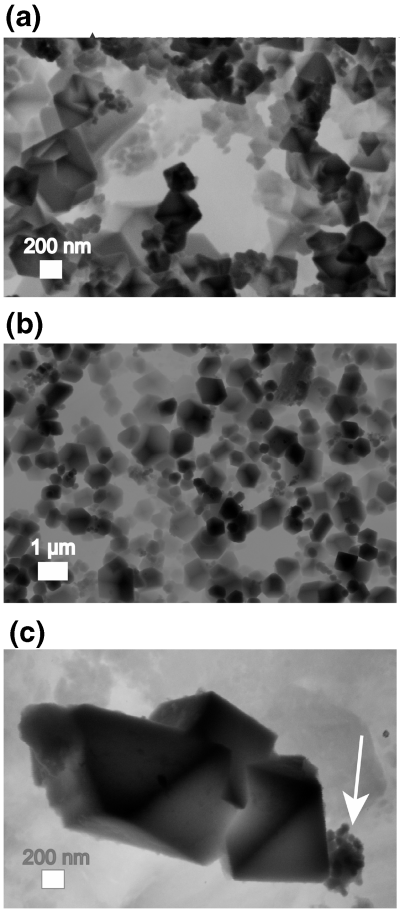

Figure 7. (a) SEM image of α-MnS formed by aging the initial MnS precipitate (precipitated at room temperature) for 3 days at 200 °C (protocol B). The morphology dominated by octahedron forms sizes ranging from tens of nanometers to 1 μm. Marker indicates 200 nm. (b) SEM image of α-MnS precipitated and aged at 325 °C and aged for 27 h (protocol A). The morphology dominated by truncated cubic forms with sizes ranging from hundreds of nanometers up to and exceeding 1 μm. The marker indicates 1 μm. (c) SEM image of α-MnS precipitated at room temperature and aged more than 20 h at 200 °C (protocol B). The morphology includes two octahedron positioned on either side of a nearly complete cube. The arrow points to crystallites with sizes on the order of tens of nanometers. The marker indicates 200 nm.

effective pore size of the filter membrane during filtration.

The PDF for the initial MnS precipitate (RT-Fresh) shows a significant degree of attenuation within ~6 nm (Figure 6). The radial distance plotted along the abscissa is extended in Figure 6 to emphasize the attenuation at relatively short distances in the RT-Fresh sample compared to more crystalline samples (Age-150 and CeO_2). Beyond 6 nm, the correlations of RT-Fresh terminate and the pattern reduces to statistical noise. This degree of attenuation is not attributable to the resolution dampening factor (σ_Q) or instrument envelope[34] but instead arises from a limited range of structural coherence in the material. This envelope is evaluated independently using a highly crystalline sample of CeO_2 having particle sizes above 1 μm. From this standard, a refined value of σ_Q is obtained that has higher intensity correlations extending to a greater radial distance than for the nanocrystalline MnS. The nanocrystalline sample with a highly attenuated PDF has a σ_Q value of 0.1, compared to that of 0.03 for crystalline CeO_2 (Table 3). Thus, from the apparent limited range of structural coherence, the minimum average crystallite size of the freshly precipitated

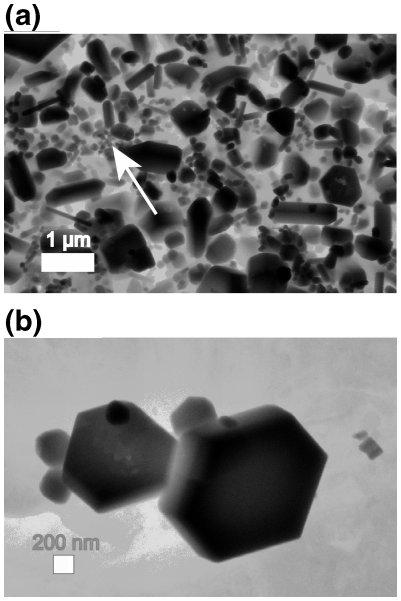

Figure 8. (a) SEM image of γ-MnS precipitated and aged at 170 °C for more than 20 h (protocol A, XRD not presented). The morphology includes many size and shape variations on hexagonal prisms and dihexagonal pyramids. Sizes range from tens of nanometers to micrometers. The arrow points to crystallites with sizes on the order of tens of nanometers. The marker indicates 1 μm. (b) SEM image of γ-MnS precipitated and aged at 170 °C for more than 20 h (same sample as Figure 8a). The morphology includes relatively large hexagonal prisms approximately 1 μm in diameter. The marker indicates 200 nm.

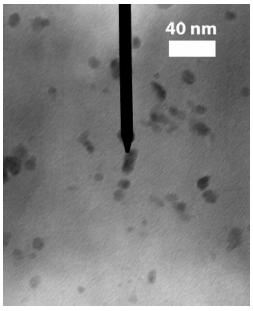

Figure 9. TEM image of the initial MnS precipitate (RT-Fresh) formed at room temperature with no additional heating or aging. The precipitate is nanocrystalline with sizes generally range from 5 to 10 nm with irregularly shaped morphologies.

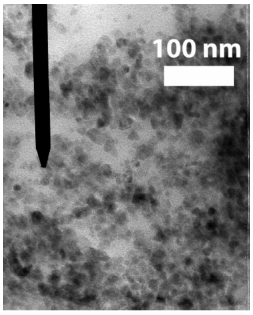

Figure 10. TEM image of the initial MnS precipitate (RT-Fresh) formed at room temperature with no additional heating or aging. Crystallites appear with relatively monodisperse sizes generally range from 5 to 10 nm and are irregularly shaped.

MnS crystallites is ~6 nm in diameter and may be greater or less in certain dimensions. This finding is consistent with TEM images (Figures 9 and 10).

Accurately determining crystallite size in natural and synthetic samples is commonly difficult to achieve by any

one method. Various methods are often employed for measuring particle sizes, for example, gas-sorption techniques (BET), microscopy, static light scattering or DLS, or small-angle X-ray scattering (SAXS). In the Fe−S system, for example, the crystallite sizes reported in the literature for an initial precipitate have ranged from 2 to 400 nm as measured and calculated using a variety of these techniques.[47] Although DLS, BET, and SAXS are statistically valid in that measurements are made over many particles, each of these techniques is of limited use in reporting individual crystallite sizes for samples that tend to aggregate in solution or as the result of processing (e.g., filtering or drying). Microscopic techniques, on the other hand, may be inaccurate because the number of particles examined is relatively low so that bias may be introduced by the observer. Recently, PDF analysis has been demonstrated as useful for determining the average particle size in nanocrystalline materials including ZnS,[43] gold,[37] and FeS.[42] The PDF technique is statistically valid because the range of structural coherence is a mass-weighted indicator of crystallite size and is not affected by the aggregation. One drawback is that, for a sample having nonuniform distribution of particle sizes, the PDF signal becomes biased toward the largest particles (bulk) because they have long-range structural coherence. In this case, the high degree of attenuation in the PDF caused by the nanosized fraction of particles may not be discernible in the presence of bulk particles.

The presence of structural disorder is also a factor that must be considered when attempting to extract particle size information from the PDF method. As discussed by Gilbert et al., a discrepancy can exist between the size of finite particles estimated from PDF and that calculated from SAXS or determined directly by electron imaging.[43] Significant structural disorder (e.g., static disorder and/or strain) is caused in part by surface relaxation and internal strain found in extremely small particles and results in a loss of structural coherence, which is reflected in the PDF.[38,43] Static structural disorder causes broadening and loss of intensity for all PDF maxima. Broadened or shifted correlations can also arise from core−shell differences in a structure that has a large fraction of atoms on or near the surface of the crystallites compared to the interior (core). The TEM images of the present study, because of their low resolution, do no help in determining if the range of structural coherence in the PDF is solely a representation of the average particle size in a population of particles or if, instead, there is a significant component of disorder present. Because the nanocrystalline sample (RT-Fresh) was adequately fit by the two-phase bulk crystalline models (Figure 4c), such disorder may not be significant. The low-resolution TEM analysis in this study constrains the particles to less than 10 nm, which is reasonably close to the 6 nm determined from PDF. High-resolution TEM will be essential to further constrain the average particle size as well as to verify the spatial relationship between the two phases (γ and β) present in the sample.

Particle size determination from DLS showed a size distribution centered on approximately 5 μm (bimodal) for the initial MnS precipitate. Populations of particles were reported with a minimum size of 0.15 μm and maximum of 10 μm. These results are consistent with neither PDF nor TEM analyses. Furthermore, nanosized particles would be anticipated in this method of synthesis because of the high supersaturation levels that result in the rapid nucleation of very small particles at the time of mixing.[42,43] The DLS technique becomes limited for determining individual crystallite sizes when there is aggregation of suspended particles in solution. Given that both PDF and TEM point to the presence of nanoscale particles, we conclude that the DLS-based distribution is likely to reflect the size distribution of aggregates in the slurry rather than the size distribution of the primary crystallites. A significant degree of aggregation was not avoided even when the pH of the solution was adjusted to a value well above its pH_{PZC}, which for MnS is less than 2.[48] DLS in this study was, therefore, not deemed to be a reliable tool for understanding the individual particle sizes of the run products.

Table 5. Analysis of Total Iron in Solids

sample ID	total iron (ppm)
RT-Fresh	1.25
Inj-250	10
Inj-350	40
reagent	**total iron (ppm)**
$MnCl_2 \cdot 4H_2O$	3.2
$Na_2S \cdot 9H_2O$	2.2

3.4. Chemical Analysis. EDAX analysis of the run products inspected by SEM confirmed manganese and sulfur as the primary components. An aluminum signal was also observed, which is attributable to the aluminum substrate of the mounting stub. A small peak, corresponding to the excitation energy of iron, also occurred, and was particularly evident in the products formed by preheating of the NaSH/NaOH solution to elevated temperature prior to mixing. Total iron content in selected run products and the initial starting reagents (Table 5) was evaluated using the UV−vis absorbance technique. For each of the three MnS samples, less than 400 mg of dry precipitate was dissolved in HCl and analyzed. The results indicate that the initial Mn^{2+} and S^{2-} reagents contain trace amounts of Fe. Incorporation of these Fe impurities in the MnS precipitate was confirmed by the analysis of the initial precipitate formed at room temperature. This sample was formed in a centrifuge tube and was never in contact with stainless steel. Leaching of iron from the 316 stainless steel vessel used in selected syntheses, particularly those conducted at elevated temperatures, was also confirmed. The heating of NaSH/NaOH solution to elevated temperatures apparently resulted in the corrosion of the interior surfaces of the vessel and the leaching of iron. The rate of leaching was apparently accelerated by increasing the preheat temperature of the NaSH/NaOH solution. The total Fe content measured in run products Inj-250 (0.001 wt %) and Inj-350 (0.004 wt %) corresponded to preheating of the NaSH/NaOH solution to 250 and 350 °C, respectively,

(47) Wolthers, M. Geochemistry and environmental mineralogy of the iron-sulphur-arsenic system. Ph.D. Thesis, Utrecht University, Utrecht, 2003.
(48) Bebié, J.; Schoonen, M. A. A.; Strongin, D. R.; Fuhrmann, M. *Geochim. Cosmochim. Acta* **1998**, *62*, 633−642.

prior to mixing. We cannot say if Fe replaced Mn in the MnS structure or if FeS was incorporated as clusters. However, in general the Fe content was minor (≤0.004 wt %).

3.5. Product Yield. The constraints on product yield vary for each protocol presented. For α-MnS formed at elevated temperature (>325 °C) using protocol A, the product yield is constrained primarily by the volume of reaction vessel and the concentration of the reagents. The total volume of the reaction vessel in this experimental setup was fixed at 42 mL, but a larger-volume vessel could also be employed. The maximum concentration of NaSH/NaOH was also a constraint in protocol A due to corrosion to the 316 stainless steel vessel, particularly when preheated to elevated temperature. The concentration of NaSH/NaOH was reduced to minimize the leaching of metal impurities (e.g., iron) from the stainless steel,[49] and, therefore, NaSH/NaOH acted as the limiting reagent. A vessel constructed of a titanium alloy (e.g., Ti-17) would be preferable to 316 stainless steel because it contains no iron and has a greater resistance to corrosion.[49] The main drawback in utilizing vessels constructed of such materials (e.g., Ti) is that cost typically increases as much as 5-fold.

The constraints on product yield in protocol B were not as strict as those for protocol A. This was primarily because the reaction of S^{2-} and Mn^{2+} forming MnS was conducted at room temperature, thereby reducing the corrosiveness of the reagent mixture by removing the majority of H_2S from solution. Hence, using a vessel constructed of stainless steel versus titanium is less critical for this protocol. The yield in protocol B is primarily constrained by the volume of the reaction vessel. By modifying protocol B to include a step in which the initial precipitate at room temperature is centrifuged to create a dense slurry, it is possible to increase the yield for a given reactor vessel considerably. In essence, by adding this step it is possible to age a larger quantity of MnS than that which can be precipitated in the reactor vessel itself. This method was successfully employed in a related study on ZnS[50] in which a ZnS was precipitated in a large-volume flask and centrifuged, the supernatant was removed, and the dense slurry was loaded into a reaction vessel for aging at elevated temperatures. In protocol B, a slight excess of sulfide was added relative to $MnCl_2$ to ensure that the solution remained reducing during aging.

4. Conclusions

Three MnS polymorphs are known, and two of these, α-MnS and γ-MnS, were precipitated as pure phases under aqueous conditions without the use of organic reagents. Direct injection techniques using two experimental protocols were employed at temperatures ranging from 22 ± 3 to 350 ± 5 °C with varying amounts of aging time. The results confirm that varying the temperature of injection and subsequent aging time, the reaction can be directed toward production of a specific polymorph.

The initial MnS polymorph formed upon mixing is dependent on reaction temperature. The predominant phase precipitated from aqueous solutions of Mn^{2+} and S^{2-} at temperatures below 250 °C has tetrahedrally coordinated wurtzite structure. At room temperature, the initial precipitate consists of a binary mixture of γ- and β-MnS. Given sufficient aging at temperatures of 200 °C and higher, the MnS makes a complete polymorphic transformation to the stable rock salt structure. MnS precipitated by direct injection at temperatures in excess of 325 °C results in the formation of the thermodynamically stable α-phase within 5 min of mixing. The γ-phase could be the initial precipitate at these temperatures, or instead it could rapidly transform to α-MnS in the 5 min prior to quenching.

A wide size distribution of MnS in both polymorphic forms was observed by a combination of techniques including SEM, TEM, and PDF in samples synthesized using both protocols A and B. Individual crystallite sizes in the samples synthesized and aged at elevated temperature ranged from tens of nanometers up to and exceeding 1 μm. Increasing the reaction temperature and aging time improved the crystallinity and increased the particles sizes. When formed at room temperature, the initial product is nanocrystalline and relatively monodisperse. This is of interest for us when evaluating nanocrystalline materials because disorder resulting from extremely small particle sizes may substantially modify the structural and chemical properties of the nanophase when compared to the bulk. PDF analysis indicates, on the basis of the limited range of structural coherence, that the average crystallite size is ~6 nm. TEM images are consistent with these PDF results. Even so, the crystallite size obtained by this combination of techniques may still be insufficiently constrained if there are other factors such as surface relaxation or internal strain that would also affect the range of structural coherence in the PDF. Observations made by SEM indicate that the morphology of the α- and γ-MnS crystals are consistent with hexagonal and cubic structures, respectively.

Acknowledgment. This study is supported by the National Aeronautics and Space Administration under Grant NAG5-13472 issued to S.T.M. and M.A.A.S. through the Office of Space Science. High-energy XRD measurements were performed at XOR 1-ID at the Advance Photon Source, Argonne National Laboratory, and made possible by the Center for Environmental Molecular Science (CEMS) and the National Science Foundation (NSF) Award No. CHE0221934 and NSF Award No. DMR-045244. Use of the APS was supported by the U.S. Department of Energy, Office of Science, Office of Basic Energy Sciences, under Contract No. W-31-109-Eng-38. Dr. James Quinn is thanked for assisting with TEM and SEM analyses. The authors are grateful for the thought-provoking discussion and assistance provided by Dr. Peter L. Lee and Dr. Peter J. Chupas of the APS and Sytle M. Antao, Dr. Brian L. Phillips, and Alexander Smirnov, all of Stony Brook University.

Appendix

The usefulness of more traditional techniques such as the Rietveld method[51] in refining the long-range atomic order of nanocrystalline materials has been limited by a broadening

(49) Ulmer, G. C.; Barnes, H. L. *Hydrothermal Experimental Techniques*; John Wiley & Sons: New York, 1987.
(50) Zhang, X. V.; Martin, S. T.; Friend, C. M.; Michel, F. M.; Ellery, S. P.; Schoonen, M. A. A. *Proc. Natl. Acad. Sci. U.S.A.* **2005**, submitted.
(51) Rietveld, H. M. *J. Appl. Crystallogr.* **1969**, *2*, 65−71.

of the Bragg reflections resulting primarily from submicrometer particle sizes.[41,52] The diffuse scattering component of the total elastic scattering from the sample, characteristic of short-range order, is usually folded into the background correction in this methodology. However, the PDF method is well-suited in that it utilizes the total scattering of the sample, that is, both the Bragg and the diffuse components, and does not assume that the structure exhibits long-range periodicity.[53] The PDF technique, originally developed to investigate the atomic order in liquids and glassy materials, has been described in detail elsewhere.[54] In brief, the PDF has peaks at characteristic distances separating pairs of atoms, and, thus, *G(r)* is a measure of the probability of finding an atom at a distance *r* from a reference atom and so describes the atomic arrangement (structure) of materials.[54]

(52) Klug, H. P.; Alexander, L. E. *X-ray diffraction procedures for polycrystalline and amorphous materials*; 2nd ed.; Wiley-Interscience: New York, 1974.
(53) Billinge, S. J. L.; Kanatzidis, M. G. *Chem. Commun.* **2004**, *7*, 749−760.
(54) Egami, T.; Billinge, S. J. L. *Underneath the Bragg Peaks: Structural Analysis of Complex Materials*; Elsevier: Oxford, 2003.

CM048320V